# Compact Mid-wave Imaging System (CMIS) for Weather Satellite Applications

Arnold C. Goldberg[a] Michael A. Kelly[a], John Boldt[a], Dong L. Wu[b], Andrew Heidinger[c], John P. Wilson[a], Kyle J. Ryan[a], M. F. Morgan[a], Jeng H. Yee[a], Jacob M. Greenberg[a] and Charles Hibbitts[a]

[a]Johns Hopkins University - Applied Physics Lab, Space Exploration Sector, 11100 Johns Hopkins Road, Laurel, MD 20723, USA

[b]NASA Goddard Space Flight Center, 8800 Greenbelt, Rd., Greenbelt, MD 20771, USA

[c]National Oceanographic and Atmospheric Administration, 1225 West Dayton St., Madison, WI, 53706, USA

## ABSTRACT

The Johns Hopkins University Applied Physics Laboratory (JHU/APL) has created a unique design for a compact, light-weight, and low-power instrument called the Compact Midwave Imaging Sensor (CMIS). Funded by the NASA ESTO Instrument Incubator Program (IIP), the goal of this CMIS development project is to increase the technical readiness of CMIS for retrieval of cloud heights and atmospheric motion vectors using stereo-photometric methods. The low-cost, low size, weight and power (SWaP) CMIS solution will include high operating temperature (HOT) MWIR detectors and a very low power cooler to enable spaceflight in a 6U CubeSat. This paper will provide an overview of the CMIS project to include the high-level sensor design..

**Keywords:** Midwave, Infrared, imaging, weather satellite

## 1. INTRODUCTION

The 2017 Earth Science Decadal Survey[1] (NSAS 2017) laid out science goals for observations of 3D winds to aid in research of atmospheric dynamics, convection and large-scale circulation that can be met with passive sensing of atmospheric motion vectors. The community increasingly recognizes that atmospheric dynamics are essential to the understanding of cloud-climate and cloud-precipitation processes, as discussed in the recommendation: "Global measurements of the spatiotemporal (four-dimensional) evolution of large-scale horizontal wind vectors are urgently needed. It is important to avoid all or nothing strategies for the three-dimensional (3D) wind vector" (NASA, 2014, 2015). The CMIS project is an effort to address this deficiency with a low-cost sensor that enables flexible accommodation on small satellites or as hosted payloads. CMIS provides a wide field of view capability for deriving cloud motion vectors that would effectively complement clear air retrievals yielded by LIDAR to potentially achieve a robust, global architecture for wind characterization.

A major uncertainty in current 3D cloud and wind measurements has historically been cloud height determination. Conventional radiometric methods rely on infrared emission at cloud top to derive brightness temperatures, which are then related to the local atmospheric temperature lapse rate to retrieve cloud heights. This method can be confounded by thin clouds in which the measured brightness temperature is heavily influenced by the underlying surface and by variable lapse rates including temperature inversions. Elaborate multi-spectral methods have been developed such as the $CO_2$ slicing method[2,3]. However, multi-layer clouds and poor specification of clear-sky radiances on a global basis can significantly reduce the accuracy of these methods.

Stereo techniques are very appealing, because they provide direct methods to derive cloud heights. Figure 1 shows the basic concept. The primary limitation of these methods is the assumption that the cloud heights are stationary over the 5-10 minute period required to obtain the multiple views with pushbroom sensing (described below). The multiple views afforded by CMIS offer the potential to eliminate the assumption that cloud heights are stationary and therefore to derive the vertical velocity of the cloud top. This is very different than NASA's MISR and ASTER instruments which also apply stereoscopic imaging techniques from the Terra satellite to perform cloud and terrain height determination. Although there is a large SWaP associated with these sensors, the community has come to recognize the unique value of stereo imaging for future cloud/aerosol remote sensing missions. The ability to provide near-exquisite measurements on

Sensors and Systems for Space Applications XI, edited by Khanh D. Pham, Genshe Chen, Proc. of SPIE Vol. 10641, 1064103 · © 2018 SPIE
CCC code: 0277-786X/18/$18 · doi: 10.1117/12.2305382

a smaller satellite and lower cost instrument would enable better persistence due to the feasibility of a larger constellation. To enable more cost-effective stereo imaging for future cloud/aerosol remote sensing opportunities, we have embarked on the development of a next-generation satellite instrument, CMIS, to meet this important science need.

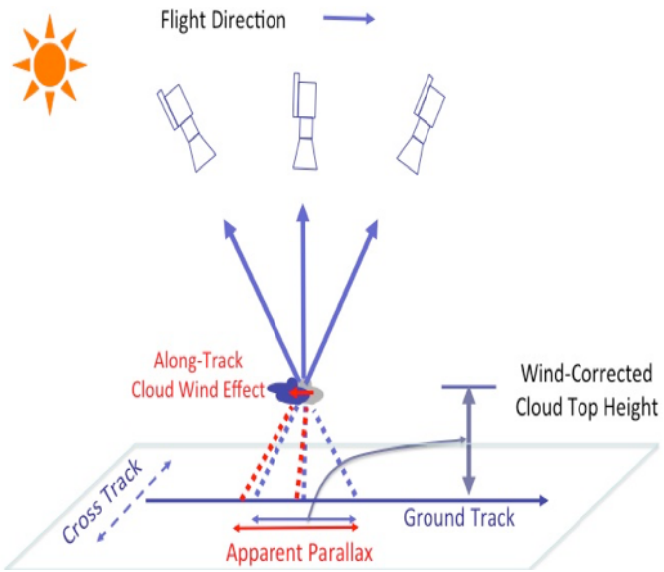


Figure 1. Cartoon illustrating the method to obtain three views of an object to apply stereo-photometric methods.

CMIS relies on detector technology that requires significantly less cooling for the detectors than similar instruments using InSb or HgCdTe (also called MCT). Without the need for large radiators or high power Stirling coolers, CMIS has a significantly reduced SWaP and can be deployed on small satellites for multiple mission applications including imaging of cloud motion vectors and physical properties including brightness temperature, cloud optical depth, and cloud fraction. Cloud properties are needed not only for climate monitoring, but also for understanding extreme wind events associated with tropical and extra-tropical cyclones and for studying multi-scale variability of clouds. Instruments that rely on the atmospheric window in the medium wave (or midwave) infrared (MWIR; 3-5 μm) have flown on numerous missions including Terra/Aqua, POES, JPSS, and GOES with utility not only for cloud remote sensing, but also for cloud-snow discrimination and fire detection. These are exquisite instruments for which their high cost limits the number of instruments that can reasonably be expected to be flown.

The philosophy for the design of CMIS was to keep the system very robust and very simple, while approaching the sensitivity and radiometric performance of Earth science MWIR instruments cooled to cryogenic temperatures. The system avoids the use of scanning mechanisms and limits the power needed for detector cooling so that the SWaP will be very low, thus permitting multiple midwave sensors to be flown for maximum temporal coverage and enabling new capabilities for investigating secular phenomena.

Until recently, only cryogenically cooled detector technologies such as InSb and HgCdTe, which require detector temperatures of <80 K were available for MWIR sensing. The detectors from CMIS are made from the newly available and continually improving high-operating temperature (HOT) MWIR detector technology based on Type II Superlattice (T2SL) detector structures. These detectors will be able to deliver similar performance as those made from the incumbent InSb and HgCdTe technology at operating temperatures near 150 K. The significant increase in operating temperature allows for use of smaller, lighter and lower power Stirling cycle coolers compared to those needed to achieve lower operating temperatures.

The CMIS project covers all aspects of the instrument design, from a detailed instrument requirements analysis to the construction, characterization, and aircraft testing of a CMIS prototype instrument, with the goal of verifying the performance of critical and technically challenging subsystems. The end result will be an innovative, low-cost, rapid-turnaround instrument uniquely qualified to meet the Earth science community's measurement objectives for cloud heights and atmospheric motion vectors.

## 2. MOTIVATION

CMIS will leverage observations from current MWIR sensors in operation but infuse the global measurements with valuable stereo information that is currently lacking, so as to enable accurate cloud height determination. Complementary to the Decadal Survey LIDAR wind mission,[4] CMIS is a building block for future cost-effective distributed systems to achieve diurnal and global coverage of three-dimensional (3D) winds.

In the MWIR, the radiance from the Earth has roughly equal contributions from solar reflected radiation and terrestrial thermal emitted radiation. Thus, in the absence of sunlight, the MWIR band has sufficient signal to measure terrestrial features at night and during the day can leverage the differences between thermal emitted and solar reflected illumination. As shown in Figure 2, cloud features are clearly evident at night when the visible band loses sensitivity. Therefore, with the MWIR and LWIR bands, CMIS will provide not only diurnal coverage, but also diurnal stereo measurements to enhance the height assignment of atmospheric motion vectors derived geostationary Earth orbit (GEO) and low-Earth orbit (LEO) platforms.

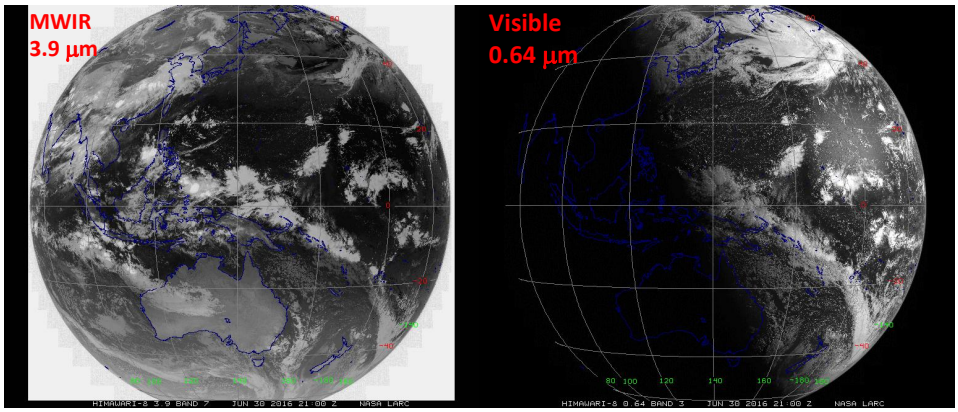


Figure 2. Himawari MWIR (3.9 µm) and visible (0.64 µm) images at 21 UTC on 30 June 2016 show the extended cloud images at night from the MWIR band.

CMIS can observe not only CGH and CMV, but also cloud-top brightness temperature. When combined with LWIR measurements, this two-point measurement of thermal radiation will enable accurate derivation of the temperature at cloud top. When combined with the stereo derivation of CGH, this will enable us to determine whether the derived temperature is due solely to cloud top emission or includes contributions from below. This new information will aid in investigation of the 3D dynamic and thermodynamic structures that impose variability on the Earth's radiation budget. Mechanisms that control cloud feedbacks on the Earth's radiation budget remain highly uncertain[5,6,7,8] so the independently derived temperature and cloud heights should facilitate a better understanding of the separate impacts of thick and thin clouds on the Earth's radiation budget. While radiometers provide exquisite estimates of the total outgoing radiation, spectral observations from CMIS can provide better global revisit because it can be flown on a large constellation at multiple local times. This capability will enable scientists to study the underlying mechanisms that contribute to variability in the Earth's radiation budget over a wider range of time scales.

The particular bands chosen for the CMIS instrument are shown in Figure 3 superimposed on a MODTRAN atmospheric transmission spectrum. The bands are located in windows where the atmosphere has high transmission. The band at 3.75 µm provides day and night (24/7) CMVs at higher spatial resolution than can be obtained with LWIR sensor on a pixel-by pixel basis (due to the smaller diffraction blur at shorter wavelengths). The band at 4.05 µm will be used to derive temperatures including those for land and sea surfaces, volcanic plumes and potentially forest fires. Finally, the band at 2.25 µm, which will only have good signal-to-noise ratio (SNR) during the daytime, will provide high spatial resolution cloud reflectivity data that will aid in the determination of CMVs and cloud typing.

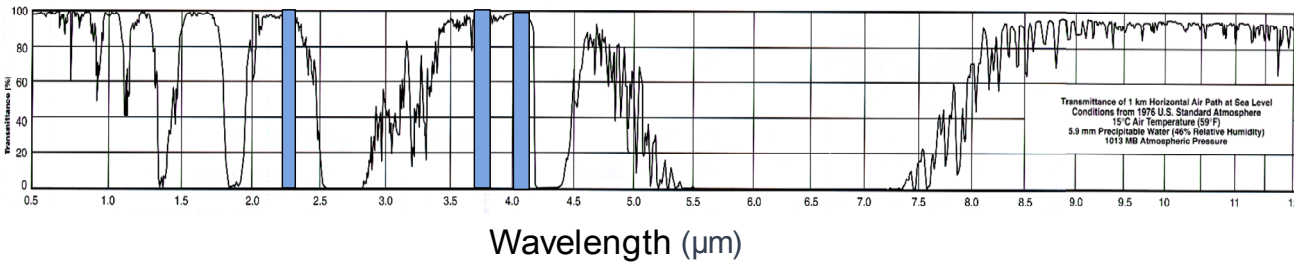


Figure 3. The CMIS bands (blue shaded) area superimposed on a MODTRAN atmospheric transmission spectrum.

There is a decided lack of 3D wind measurements in the Tropics where the assumption of thermal-balanced winds are invalid. The dynamical couplings between different tropical cloud processes (e.g. convective, congestus, and stratacumulus clouds) are poorly understood. Although geostationary satellites provide nearly continuous coverage over the Tropics, the transition between different cloud regimes in the Tropics is strongly dependent on the large-scale atmospheric circulation. This suggests that CMVs and CGHs contributed by CMIS could be more effective in elucidating the transition between tropical cloud regimes because of the improvement in height assignments of the atmospheric motion vectors as compared to geostationary satellites (e.g. GOES).

To fit the MWIR imager into a 6U CubeSat, it requires a very small SWaP as stated above. Until now, the need for a high-power Stirling closed-cycle cryocoolers for sensor cooling has made it very difficult to fit the sensor within the space and weight constraints of a CubeSat. However, the latest generation of HOT MWIR detectors and newer, efficient and small footprint Stirling coolers have now made it possible to fit a highly capable sensor into a package the size of a 6U CubeSat. In addition, the reliability of modern Stirling coolers is much improved over those from several years ago such that mean time to failure (MTTF) can allow for much longer lifetimes in orbit.

## 3. DETECTOR TECHNOLOGY

Initially, we had planned to use detector arrays based on lead selenide (PbSe) which had been developed in recent years for threat warning sensors. These detectors offered the possibility of operating at temperatures within the reach of thermoelectric (TE) coolers which have the advantage of no moving parts (high reliability), small size and weight as well as low cost compared to Stirling cryocoolers. However, early in the program it proved to be that the PbSe detector technology was not mature enough for us to procure FPAs from a commercial vendor in the program's time frame. In addition, to meet the sensitivity goals of the program the PbSe FPA needed to be cooled to 230 K (-43 °C) which is at the limit of current two-stage TE cooler technology. To maintain this operating temperature the TE cooler would need to draw significantly more power from the vehicle than a small Stirling cryocooler providing an operating temperature of 150 K. Therefore, we switched the procurement strategy from PbSe to the Type II Superlattice detector structure. Recent results showed excellent radiometric performance of T2SL detector arrays operating at 120 K for a cutoff wavelength of 5.2 μm. Well-established performance models predicted that similar performance could be expected at an operating temperature of 150 K for devices with a cutoff wavelength of 4.2 μm.

### 3.1 Type II Superlattice Detectors

Over the last several years there has been rapid development in detectors for MWIR and LWIR using artificial Superlattice structures containing alternating layers of various III-V compounds (e.g. InAs, GaAs, AlAs, GaSb and their alloys). The original Superlattice concept put forth by Esaki and Tsu in 1970[9] structures were made using GaAs and $Al_xGa_{1-x}As$ which are very well lattice matched to each other for values of $x$ below 0.4. In these structures the offset of the conduction band and the valence band both go toward higher energies at the interface between the small band gap (GaAs) and the larger band gap ($Al_xGa_{1-x}As$) material. This is known as a Type I Superlattice and is shown schematically in Figure 4a. It is possible with this material structure to create energy levels in the quantum wells of the Type I superlattice that are separated by energies on the order of 0.1 to 0.2 eV which can absorb IR photons. This is the basis for the Quantum Well Infrared Photodetector (QWIP) that was put forward in the mid-1980s as an alternative to MCT for LWIR imaging. However, the quantum mechanical selection rules forbid absorption of normally incident IR photons in this structure. Therefore, diffraction grating structures are required to be fabricated on each pixel to scatter normally incident light into the correct polarization for absorption. As a result the conversion efficiency of these devices (which are high resistance photoconductors) is quite low compared with MCT and other band-to-band absorption

photodiodes. Even so, QWIPs proved to be a viable alternative for LWIR imaging systems for certain applications. Other material combinations cause the bands to offset in opposite directions at the interface such that the top of the valence band in one material can be below the edge of the conduction band in the other material. Such a band alignment, known as a Type II superlattice, is shown in Figure 4b. With the Type II band alignment the conduction band electrons and the valence band holes may be separated by a relatively small amount in energy but they are spatially separated in alternate layers of the superlattice. However, the spatial separation is still within the region where there is significant overlap of the wave functions associated with the electrons and holes. Therefore, there is a high probability of absorption of photons with energies at or above the energy difference between the "minibands" defined by the superlattice. In addition, the miniband created in the conduction band provides a conducting channel for the electrons which the holes remain localized under an applied bias due to their much higher effective mass. With appropriate doping these T2SL structures can be grown as photodiodes and operated in a very similar manner to HgCdTe or InSb photodiodes. Since the photon absorption creates electron-hole pairs in different bands, normally incident light is easily absorbed.

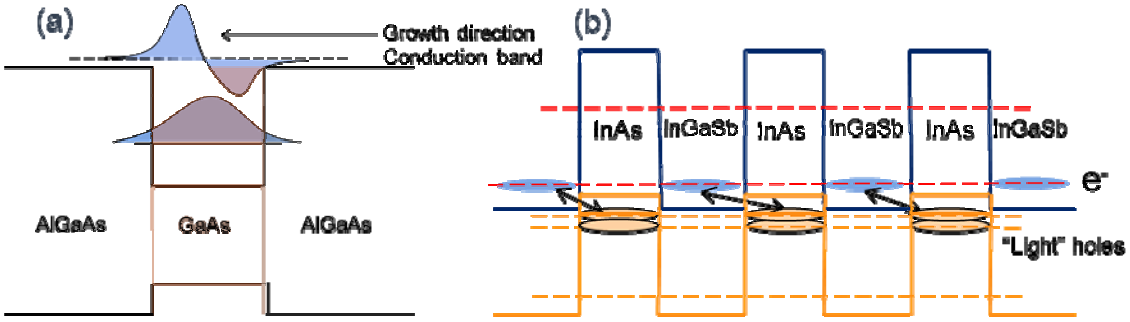


Figure 4. Type I (a) and Type II (b) band alignments for superlattice structures.

When T2SL structures were initially proposed it was recognized that the properties of the underlying III-V materials and the artificial structures created using molecular beam epitaxy (MBE) would act to suppress the Auger VII recombination process which is responsible for most of the dark current in HgCdTe photodiode structures. However, it took several years of work, most notably on surface passivation of the T2SL material to produce detector structures that realized this dark current advantage. Recent published data shows dark current levels for MWIR (5 µm cutoff wavelength) at a factor of 2.3 above the "Rule 07"[10] level predicted for the best HgCdTe detectors and at as much as 2 – 3 times *lower* than that predicted for HgCdTe for LWIR (12 µm cutoff wavelength). Thus, it is expected that a MWIR T2SL detector with a 4.2 µm cutoff wavelength should have low enough dark current at an operating temperature of 150 K to have the radiometric performance necessary for CMIS.

### 3.2 Other Detectors Considered for CMIS

It is worth mentioning that we did consider other detector modalities for the CMIS sensor. As mentioned above, our original idea was to use PbSe detectors which had been shown to have acceptable performance for an operating temperature of 230 K but that the detectors had proved to not be available with sufficient quality in the time frame necessary for this program. An alternative detector structure that was considered was the so-called nBn or Barrier Layer detectors which have been developed to high quality over recent years. The band structure for a typical nBn detector is shown in Figure 5. Electron-hole pairs are created in an absorbing layer with a band gap appropriate for the desired cutoff wavelength. The materials for the absorbing layer and barrier layer are chosen such that there is minimal discontinuity in the valence band but a large discontinuity in the conduction band. A sufficiently thick barrier layer will block nearly all conduction of photo-excited electrons from passing between the ohmic contacts while the holes created by photon absorption pass relatively unimpeded by the barrier between the contacts. The barrier also blocks the flow of dark current electrons and thereby reduces the dark current relative to a similar detector without the presence of the barrier. From a radiometric and dark current perspective the T2SL and nBn detectors had basically equivalent levels of performance for the 4.2 µm cutoff wavelength desired for CMIS.

In the end, after an evaluation process that included considerations of detector performance, availability and cost we decided to procure T2SL detectors hybridized to a 640×512 readout integrated circuit (ROIC) with a pixel pitch of 15 µm (FLIR ISC0403[11]). The detectors are expected to be delivered in May 2018.

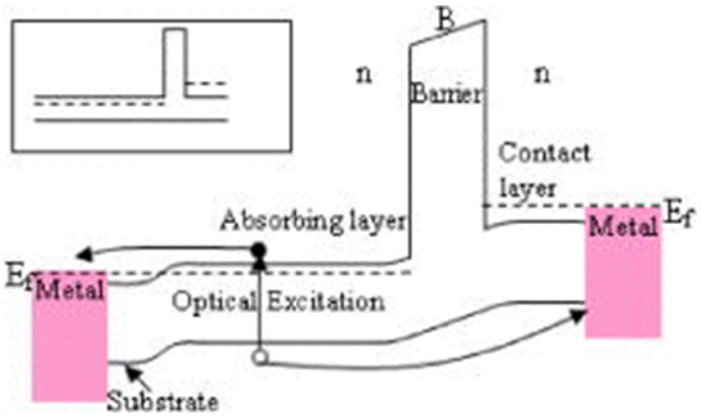


Figure 5. Typical nBn structure that allows the flow of photo-excited holes between contacts while blocking electrons.

## 4. COOLER TECHNOLOGY

The initial intent of the CMIS effort was to use detectors for which TE coolers would provide sufficient cooling. However, with the shift from lead salt based detectors toward T2SL or other III-V material based detector technology we had a need for a Stirling cycle cryocooler that would cool the detector to 150 K and with sufficient heat lift to maintain that temperature for the detector and the other optics hardware (filters, cold shield, etc.) in the dewar with sufficient stability. There have been concerns expressed about the use of cryocoolers in spacecraft because of the perceived lack of reliability relative to TE coolers or passive (radiative) cooling which involve no moving parts. In addition, Stirling cryocoolers can draw a significant amount of power from the spacecraft bus and they have traditionally also taken up amounts of space and weight that made them inappropriate for uses in small satellites like CubeSats. However, in the last few years cryocoolers have become more energy efficient, smaller and lighter, especially for applications that only require cooling to temperatures ~150 K. JHU/APL conducted an evaluation process for several candidate cryocoolers and we were able to identify a prime candidate unit that uses the integral rotary design with the properties given in Table 1.

Table 1. CMIS Cryocooler Properties.

| **Property** | **Value** |
|---|---|
| Weight | 470 g |
| Cooling Capacity | 500 mW at 77 K cold end temperature to 71 °C ambient. |
| Mean Time to Failure (MTTF) | 30,000 hours (3.42 years) |
| Input Power | 2.0 Watt for 300 mW lift to a 23 °C ambient |

JHU/APL used similar cryocoolers in the Compact Reconnaissance Imaging Spectrometer for Mars (CRISM) instrument that is still flying on the Mars Reconnaissance Orbiter (MRO) which was launched in 2005. Unlike previous MWIR imaging missions which required detector cooling to <100 K, the required operating temperature of 150 K allows for the cooler to be run at considerably less than its full cooling capacity which reduces the input power needed to run it and is expected to lengthen its lifetime.

## 5. OPTICAL DESIGN

To meet instrument performance goals, a preliminary design for a high-speed, wide-field, imaging lens with 5 elements was developed, as shown in Figure 6. The 11mm focal length provides a 40° by 50° field of view over the detector at a focal ratio of f/1.2. An achromatic design provides reasonable correction from the SWIR to the MWIR bands. Selective vignetting has also been employed to reduce the overall size of the optics and balance performance across the field. Total distortion was also limited as much as possible (approximately 12% over the full field) to support real time image

correction for time delay and integration. The result is a nearly diffraction limited system with sufficient margin to meet requirements after assembly.

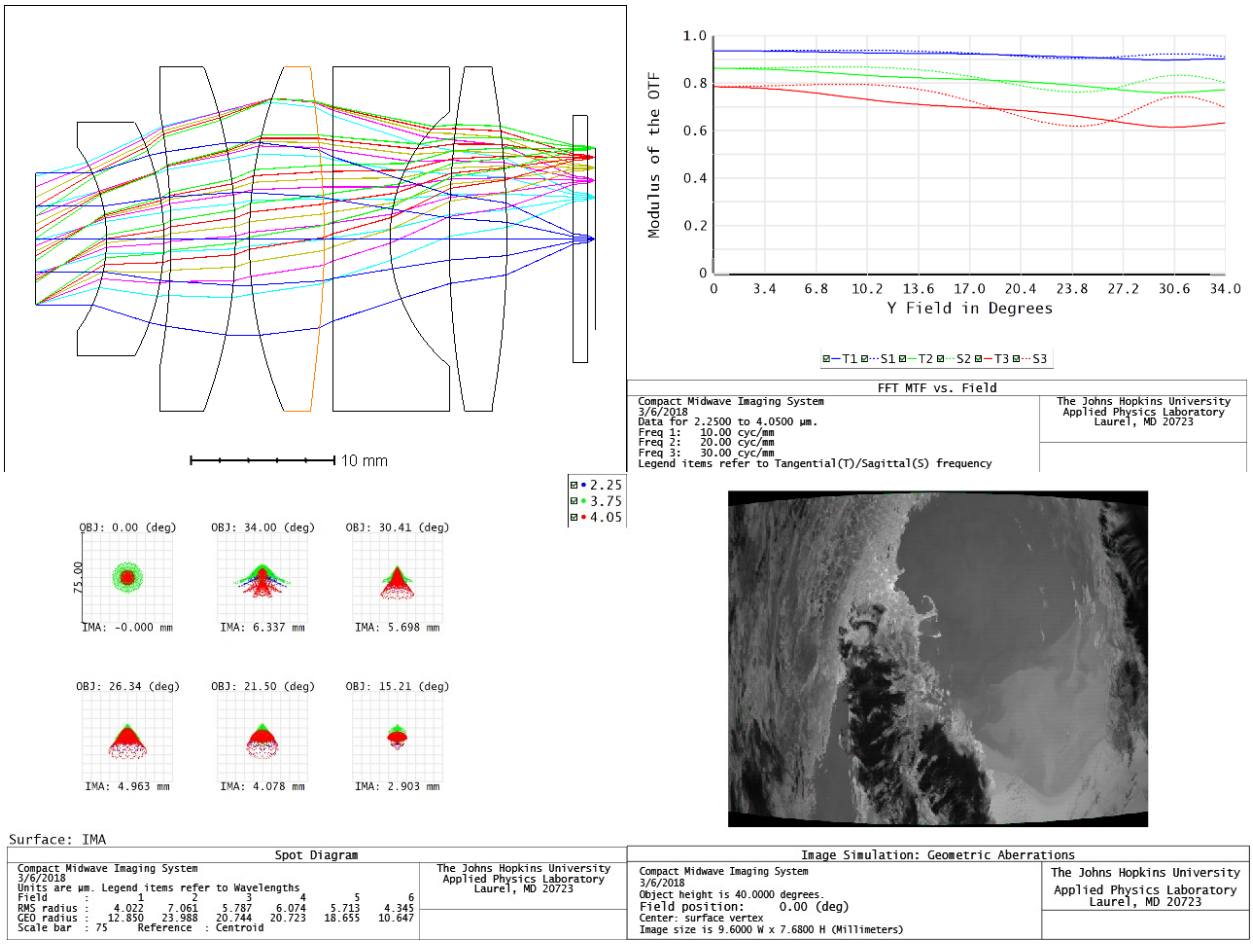


Figure 6. Layout and performance summary of the CMIS optics. Clockwise from left: cross section and ray trace (including filter array at right), modulation transfer function across the field at selected spatial frequencies, and spot diagram (grid represents ½ of a pixel), and a simulated image demonstrating distortion.

The use of interference filters at the focal imposed a significant design restriction, as telecentric illumination was required to eliminate blue shift across the field of view. This prevented the use of a traditional cold stop arrangement, as the exit pupil is located at infinity, giving the detector full view of all the optics and the structure, requiring them to be cooled to minimize background signal. Therefore, the system has been made with the stop at the front to minimize exposed area, and the entire assembly restricted in size to fit within the dewar. An advantage is the optical system is maintained at constant temperature when on orbit, eliminating the need for athermalization. The images at the bottom left of Figure 6 show how well a point source is imaged in the 3 bands at different incident angles of the light with respect to the normal to the focal plane with each small square represents ½ pixel. This shows that the optical design transfers a large fraction of the light even at the edges of this relatively wide field of view. The image at the bottom right of Figure 6 shows a simulated image of a terrestrial scene from orbit. There is noticeable distortion at the edges of the image but the level of distortion is small enough that a high fidelity image of the original scene can be reproduced with straightforward image processing techniques (as described in the Performance Prediction section below).

The filters positions and bandwidths that were chosen were based on the science presented above and they are to be incorporated into a "butcher block" configuration in which 5 filter strips are placed close together just above the FPA and cooled to the same temperature as the FPA to reduce thermal emission. Actually, all of the optical elements will be thermally connected to the closed-cycle cooler so that they will be at temperatures near that of the FPA. The band at 3.75 µm will provide the majority of data from CMIS as it is key to the science objectives. Figure 7 is a schematic

representation of the stripe filter design. Three of the 5 filter strips that are to be installed above the FPA will be in the 3.75 µm band while 2.25 µm and 4.05 µm bands will each have 1 stripe dedicated to them. Since the FPA will have a 640×512 pixel format each of the strips will have slightly less than 100 rows of pixels associated with it. The full conceptual design using telecentric optics and a Stirling closed-cycle cooler integrated with a dewar is shown in Figure 8.

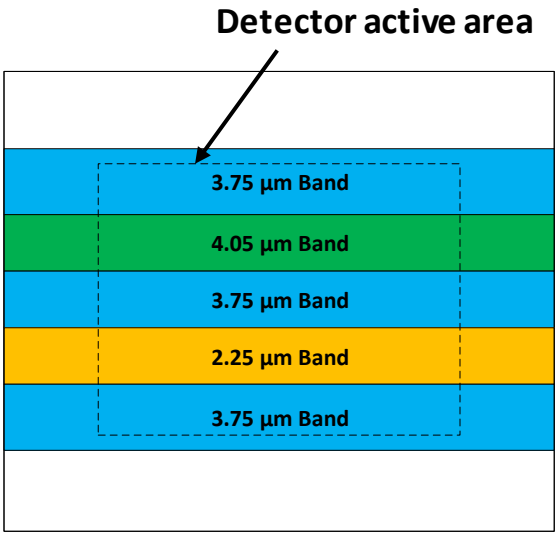


Figure 7. Stripe filter concept with fore, nadir and aft views at 3.75 um for stereo imaging along with stripes for imaging at 2.25 µm (orange) and 4.05 µm. The dashed-line rectangle shows the active area of the 640×512 FPA.

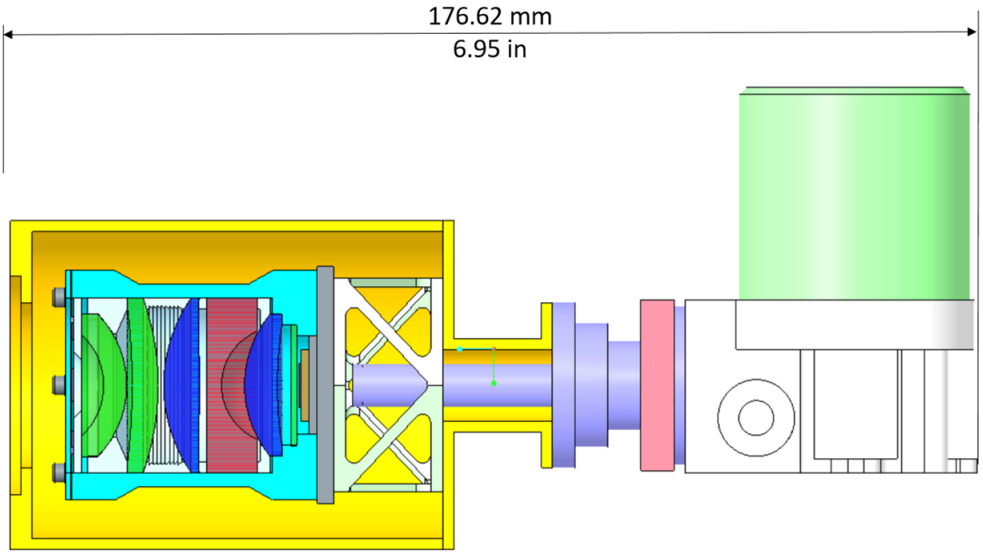


Figure 8. Conceptual optomechanical configuration for the CMIS instrument integrated with the cooler.

## 6. CONTROL ELECTRONICS AND DATA HANDLING UNIT

The CMIS instrument is being designed specifically for integration to a spacecraft for on-orbit observations. Therefore, all of the electronics including the command and control electronics (C&CE) for the FPA, the closed-cycle cooler and the shutter/calibration mechanism (to name a few of the subsystems) are being designed to use components that have flight heritage and to fit in the small form factor envisioned for the instrument. While the initial airborne demonstration

may not have all of the space-qualified components that would be used on an actual satellite, they will be functionally equivalent. The C&CE for the FPA will provide the clock signals and bias levels to the ROIC and will digitize the output signals from the FPA's analog outputs. The electronics for the CMIS instrument will be segmented into essentially 3 circuit boards, the detector electronics board, the power electronics board and the digital electronics board.

### 6.1 Detector Electronics Board

A block diagram of the detector electronics board is shown in Figure 9. The physical input/output (I/O) to the FLIR ISC0403 ROIC can be accomplished with as few as 14 interconnections to the dewar and a standard 25-pin connector can handle all of the possible I/O connections. The current design for the detector electronics allows for individual tailoring of all bias and power inputs, and includes provision for use of two ROIC video outputs (CMIS frame rates require allow use of a single output). The detector electronics board includes digital-to-analog converters (DAC) for setting bias levels and high-speed 14-bit analog-to-digital converters (ADC) to convert the analog output signals to digital values for image processing.

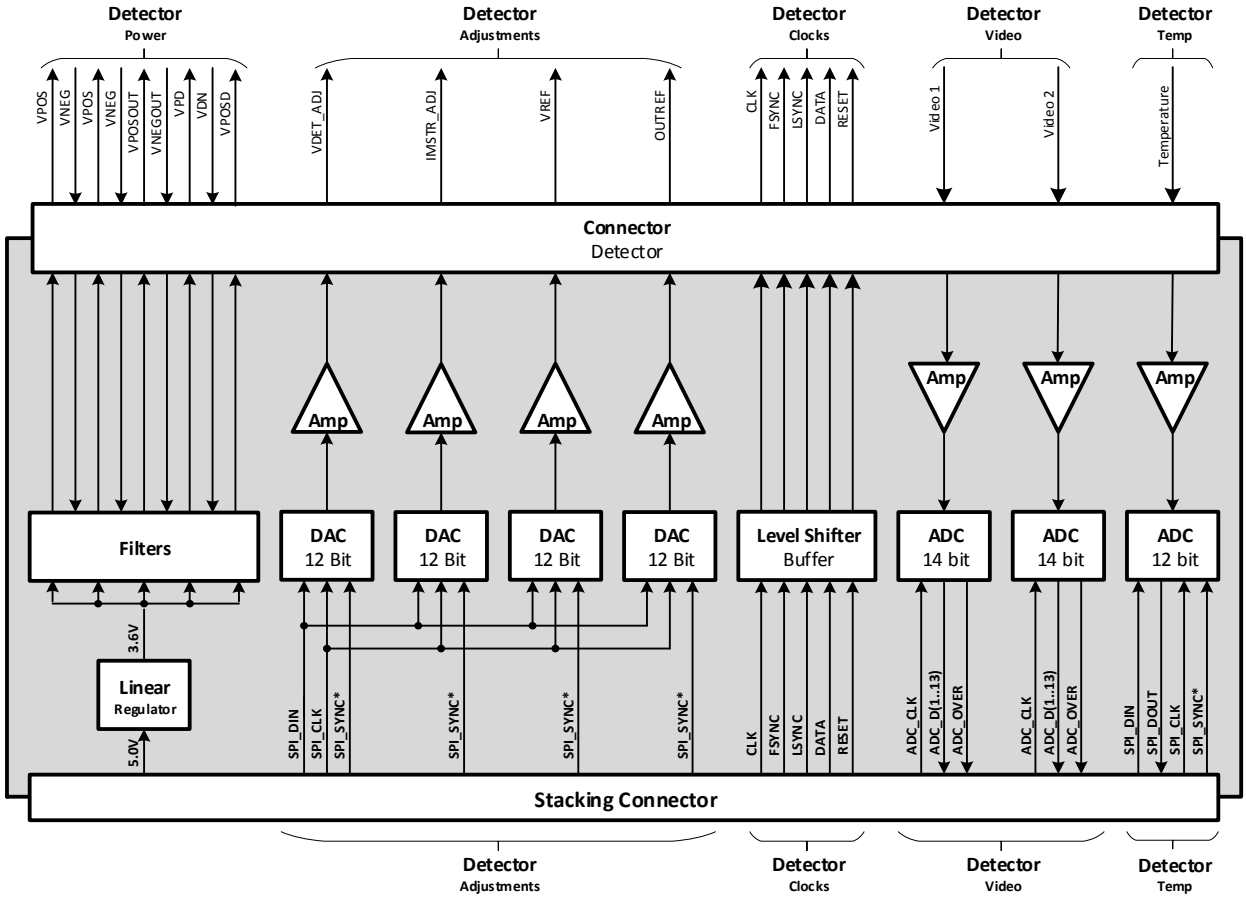


Figure 9. Block diagram of the detector electronics board.

### 6.2 Power/Interface Electronics

A block diagram of the power/interface electronics board is shown in Figure 10. All of the I/O connections for the instrument will be located on the power board which will be located at the rear of the camera. The connectors on the power board will be matched to connectors on the detector electronics and digital electronics boards in a stacked architecture. The connectors, drivers and receivers on the board can be configured to run in a high-bandwidth SpaceWire interface or in a low-bandwidth asynchronous interface (which is required by some CubeSats). The DC/DC power converters have been chosen to be magnetically isolated with either 28 V or 12 V inputs. The specific voltage would be determined by the host satellite bus requirement.

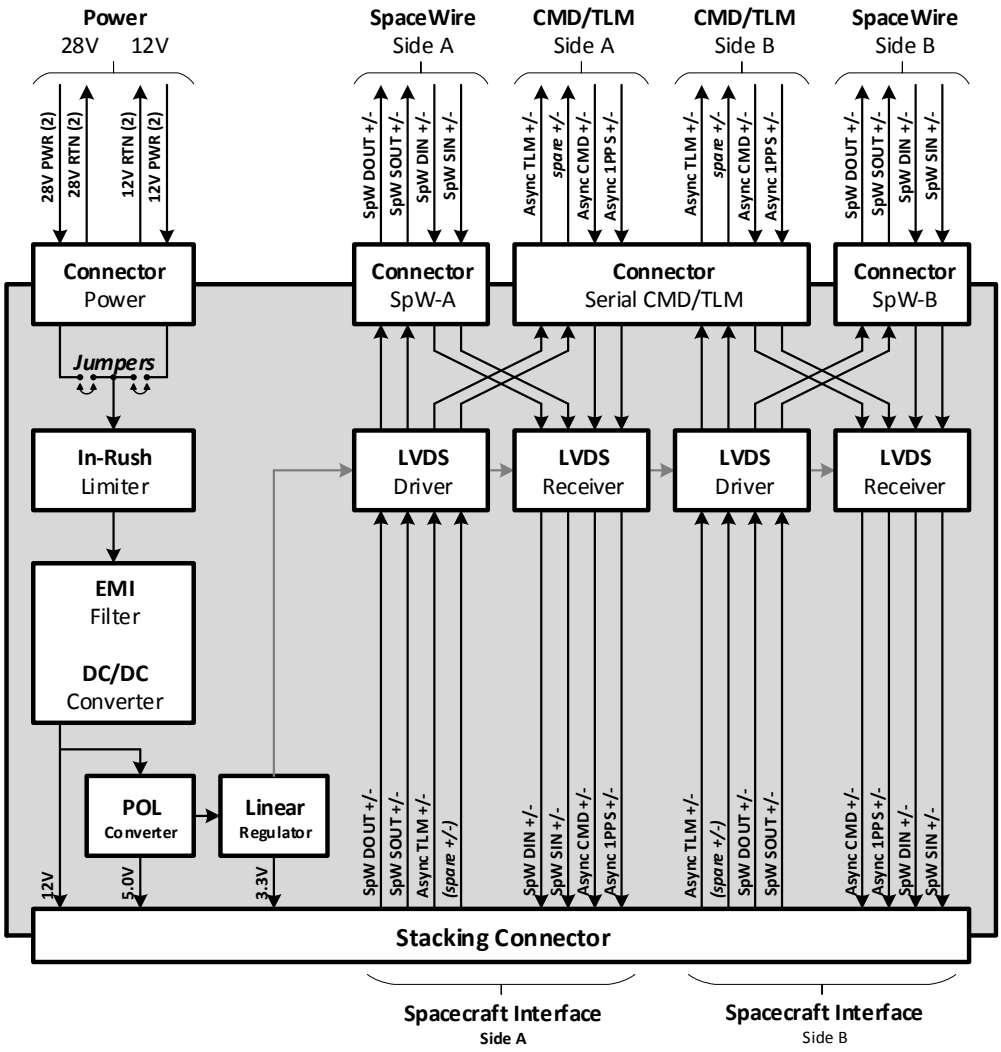


Figure 10. Block diagram of the power/interface electronics board

### 6.3 Digital Electronics Board

A block diagram of the digital electronics board is shown in Figure 11. This board contains the field-programmable gate array (FPGA), on-board memory chips plus voltage regulators as needed. The FPGA holds the embedded software to run the camera and perform the image processing functions including nonuniformity correction (NUC) and digital TDI and distortion correction. Three types of solid state memory chips have been chosen to be used on the CMIS digital board. Non-volatile Magnetoresistive Random Access Memory (MRAM) flash RAM and SRAM. The final configuration of the memory will be optimized to use as little power as possible.

The three principal image processing functions listed above will be accomplished on the digital board as follows:

- NUC: Perform running sums in memory of "low" and "high" signal data followed by calculation of 8-bit gain and offset coefficients for each pixel which are then stored in non-volatile memory. This would require 5.2 Mbits of nonvolatile memory. If it is determined that 16-bit gain and offset coefficients will be necessary the total storage allotment would grow to 10.4 Mbits. The NUC process need not run at the full data rate of the detector.

- Digital TDI: Perform running sums in memory at the full data rate of the detector with co-adding of 4 consecutive frames (for a 2× increase in SNR). This would require approximately 20 Mbits of SRAM (volatile) memory.
- Distortion correction: The optical system will produce a somewhat distorted image of the scene, especially near the edges of the field of view. We have developed algorithms to correct for this distortion that will be programed into the FPGA. The algorithm uses a 4-pixel bilinear interpolation, 4× read-multiply-add followed by a division (bit shift) and requires the calculation of 6 coefficients, 4 4-bit pixel weights and 2 8-bit pixel offset values which will require 2.45 Mbits of non-volatile memory.

All of these functions can easily be performed with current FPGA and memory technology in the space allowed.

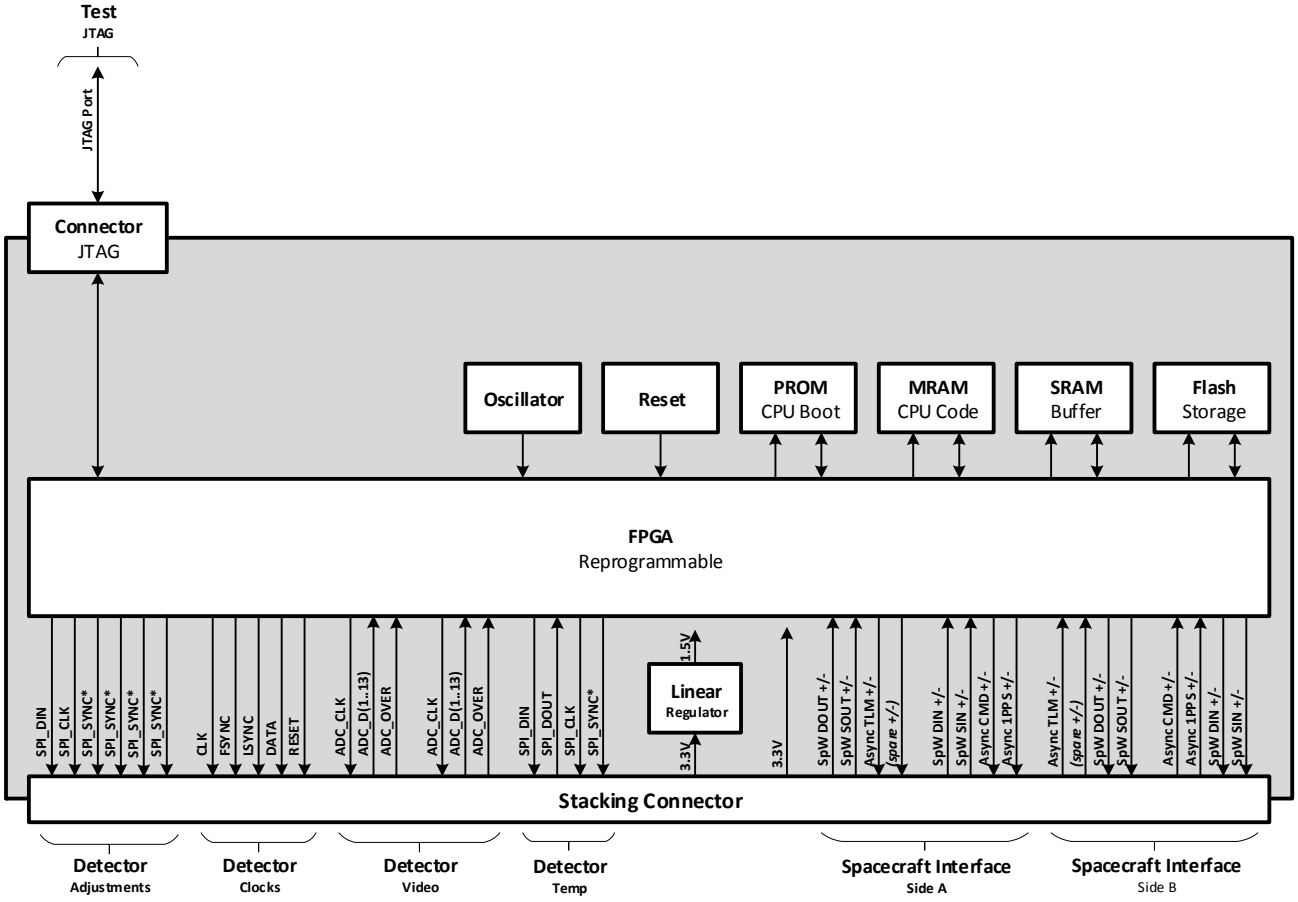


Figure 11. Block diagram of the digital electronics board.

## 7. PERFORMANCE PREDICTIONS

The CMIS concept is driven by the desire for a large FOV (both along track for better stereo measurements and cross track for coverage) and high SNR. The optical system described earlier provides the large FOVs with the light collecting capabilities of a low f/# system. Combined with the low noise performance of the selected detector at the operational temperature of 150 K results in a system capable of producing a low noise image over a large swath. The instrument is simple enough to fit on a 6U CubeSat which allows for flexibility in mission design. The sensor could be flown on a standalone satellite or hosted on a larger satellite. As a sample concept of operations, an altitude of 800 km is assumed for analysis purposes and to allow for comparisons to MODIS data. The data in Table 2 shows the performance characteristics of the CMIS sensor at this altitude while Figure 12 shows the graphical representation of this FOV from the given altitude. Here it is assumed that the sensor is operating in pushbroom mode and uses three lines from the full frame sensor to produce three separate images: fore, nadir, and aft. These three images are combined using stereo

photogrammetry techniques to measure the geometric height of clouds within the FOV of the sensor. In addition to these three views, block filters are added to the center of the detector to produce multi-spectral imagery.

Table 2. Performance at 800 km altitude

| Parameter | Value |
|---|---|
| Swath | 756 km |
| GSD at Nadir | 1.1 km |
| Stereo angles | +/- 20 ° |

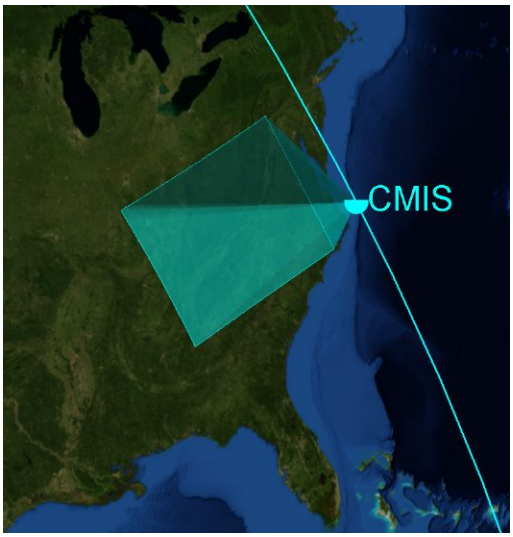


Figure 12. Image of the CMIS sensor FOV from an altitude of 800 km

The signal to noise performance of the sensor is calculated based on dark current measurements and standard model predictions for a device temperature of 150 K, read noise discussed earlier and shot noise. The integration time of the sensor is limited by the orbital speed and IFOV to limit smearing. For the altitude of 800 km, an IFOV of 1.4 mrad, the integration time is limited to 6.7 ms to avoid the sensor footprint from moving by more than 1/10 of a pixel. The noise-equivalent temperature difference (NETD) of the sensor is calculated based on these assumptions and plotted in Figure 13 as a function of input radiance from an ideal blackbody over a range of temperatures that span the typical range for cloud top brightness values. Even for high altitude cirrus clouds (~230K), the NETD of the sensor provides low noise performance. Further enhancement of signal-to-noise ratio (SNR) and consequently reduction of the NETD can be achieved through time delay and integration (TDI) techniques that will ensure that a temperature measurement accuracy of 1 K or better can be achieved for target temperatures as low as 230 K.

As was shown in the picture at the bottom right of Figure 6 the imaging system is expected to produce some image distortion near the edges of the field of view. The on-board data processing unit will be used to correct the distortion using a bi-linear algorithm. The algorithm was tested in MWIR imagery from MODIS using Matlab. Figure 14 shows the results of applying the distortion correction. The Truth Data (center) was distorted using the known properties of the optical design to producing the Distorted Image (left). After the distortion correction algorithm was applied the Corrected Image (right) was produced which was virtually indistinguishable from the Truth Image.

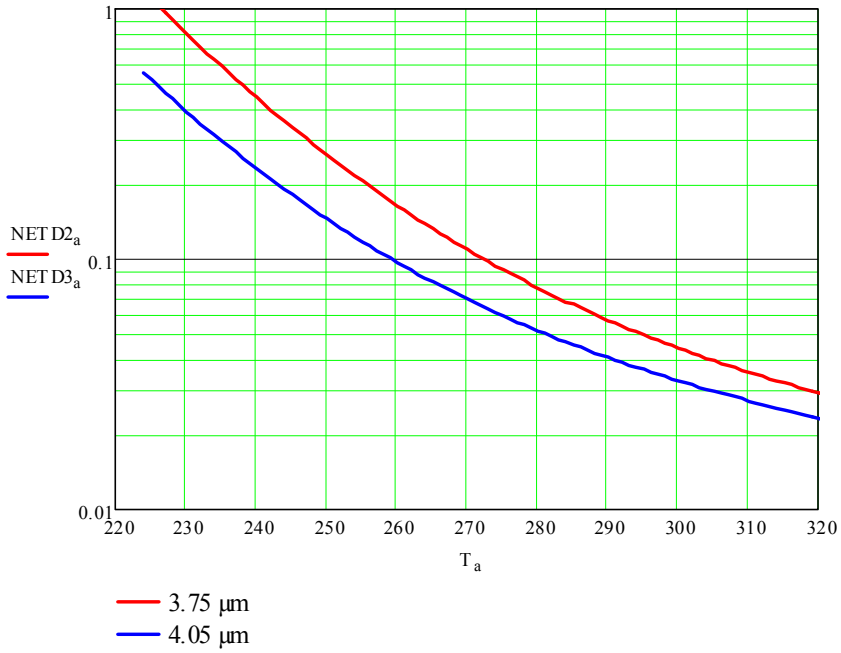


Figure 13. The predicted NETD of the sensor over typical cloud top temperatures.

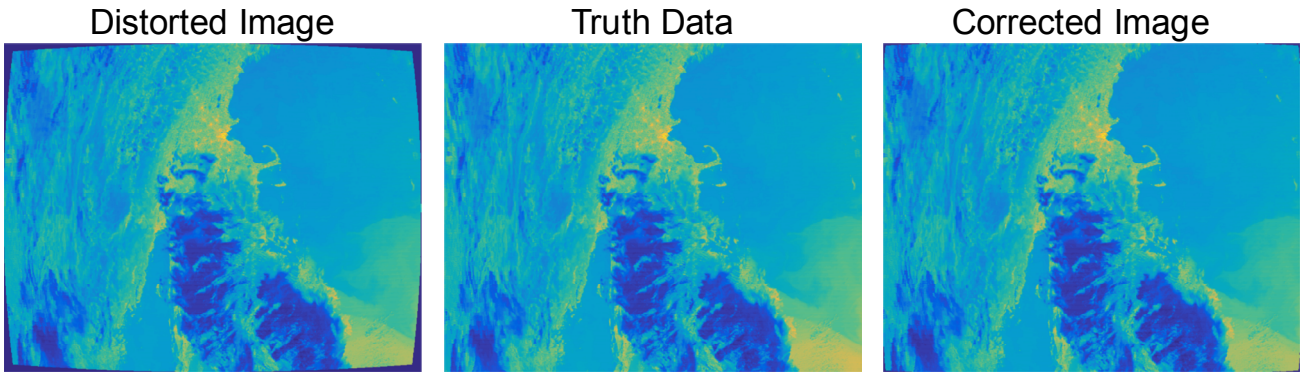


Figure 14. Demonstration of the distortion correction to be used on CMIS using MODIS MWIR imagery.

## 8. CALIBRATION

In its introduction the NIST publication Guidelines for Radiometric Calibration of Electro-Optical Instruments for Remote Sensing states "State of the art, remote sensing electro-optical sensors being designed for today's space-based applications require thorough radiometric calibrations to characterize the instrument and to ensure that all mission objectives are met."[12] The case of the imaging sensors on the CMIS spacecraft will be no different and an effective calibration strategy both on the ground (lab) and in flight (airborne and eventually in space) will need to be developed to ensure that CMIS meets the science goals that have been set for it. The calibration procedure must include measurements (using instrumentation which is traceable to NIST) of the spectral transmission of all optical elements individually as well as the optical system as a whole once it is assembled. In addition to those measurements, the performance of the CMIS FPA in terms of quantum efficiency, dark current and overall system noise will need to be made over a range of operating temperatures that are expected for the final instrument. The targeted detector operating temperature is 150 K but performance measurements are planned for operating temperatures ±10 K from the nominal value. From the radiometric performance measurements the noise-equivalent temperature difference (NETD) can be calculated. As shown in Figure 13 the NETD is expected to be a function of the background temperature such that at low background temperatures the NETD is higher than at high background temperatures. On the ground (in the

laboratory) we plan to make extensive measurements of the detector performance both before integration with the cooler, dewar and optics and following integration as a full sensor unit.

Other optical performance properties such as the modulation transfer function (MTF) which describes how well the optics image point sources and closely spaced objects will be measured. The calibration measurements on the ground will take place in APL's Optics Laboratory which contains the following equipment:

- Infrared collimator with integrated blackbody source (12 in diameter f/6)[13]
- Low-temperature extended area blackbody source (-40 °C - +100 °C)[14]
- Integrating sphere (for calibration of the 2.25 μm band).[15]
- Monochromater capable of producing monochromatic light from 1.2 μm to 12 μm.[16]
- Commercially available IR FPA drive electronics hardware and software.[17]
- Variable temperature liquid nitrogen flow-through cryostat with cooled filters.[18]

In addition to the measurements at several detector operating temperatures the laboratory characterization will be done over a wide range of other sensor operating conditions such as frame rate, integration time and detector bias.

This procedure will be sufficient to calibrate the instrument in the 3.75 μm and 4.05 μm bands where there is sufficient flux from the background at terrestrial temperatures to be in the background limited infrared performance (BLIP) regime. However, at 2.25 μm the thermal emission from the background is several orders of magnitude lower than at the longer wavelengths. For this band a radiance source such as an integrating sphere will be used to simulate the reflected sunlight from clouds for the ground calibration. We will perform response and noise measurements over a wide range of possible operating conditions to fully characterize the performance in this band as well.

In preparation for our initial design review we considered several approaches for in-flight calibration of the sensor. For any IR sensor it is necessary to do a NUC due to the inherent spread in both gain and offset of the individual detectors in the FPA. Typically, a 2-point NUC is sufficient to produce imagery with less than 0.5% spatial nonuniformity at the background flux levels used for the NUC. Spatial nonuniformity, also known as fixed-pattern noise – will be present to some degree at flux levels higher or lower than those used for the NUC and it has been found that IR sensors need to have the NUC repeated on a regular basis to minimize this effect. IR sensors using microbolometers have been found to have the need for very frequent NUC (i.e. every 5 minutes). Those using HgCdTe may be able to go several hours between NUCs if the device temperature is sufficiently stable and the photocurrent due to background flux is much greater than the dark current. Sensors made using quantum well infrared photodetectors (QWIPs) have been found to have the most stable NUCs lasting several months with no significant changes. We expect that the Type II Superlattice FPA will have NUC longevity significantly longer than that for HgCdTe but probably less than that for QWIPs. Since to our knowledge detectors made from Type II Superlattice structures have never been flown in space before we do not have any previous data on which to base this conclusion and so the longevity of NUCs in terms of the amount of fixed-pattern noise that enters the imagery as a function of time from the last NUC will be one of our planned measurements.

Our notional design for doing NUCs in flight will include a shutter over the primary aperture of the instrument onto which a thermoelectric cooler (TEC) with a high emissivity coating is integrated. This will allow temperatures below the spacecraft ambient to be presented to the detector. The TEC becomes a heater when the bias on it is reversed thus allowing temperatures above the ambient to be used for NUC. The temperature of the TEC surface can be controlled very tightly (<0.05 °C) using a PID controller. Currently, we are in the process of determining what temperature range is available for hot and cold sources based on the power that could be made available to the TEC and the PID controller.

The approach for NUCs using different temperature sources on a shutter will not work for the 2.25 μm band. For the detectors in this band an alternative NUC approach using signals collected at different integration times is very effective and is the most likely NUC method to be used. Since the flux from the range of terrestrial temperatures is insufficient to produce reliable signals in the 2.25 μm band, other sources must be used for in-flight calibration. Two possible candidates for calibration sources in this band are Pseudo Invariant Calibration Sites (PICS)[19] on the ground or the moon and/or stars. Since the instrument is designed for use as a nadir looking sensor observations of astronomical objects would require moving the spacecraft which may present some challenges to the platform. However, if the satellite could be put into a relatively slow roll about its orbital velocity axis (10 minute period) there would be several opportunities to observe bright celestial objects during a day with the object contained in the 640×100 pixel region of the field of view for more than 78 s in each viewing. Care would need to be taken that the shutter would be closed during times when the sun could enter the field of view but as shown in Figure 15 high SNR imagery of the moon can be attained. Another

calibration method would be to time the CMIS observations with observations of the same points on the ground simultaneously with other platforms thus providing on-orbit cross calibration.[20]

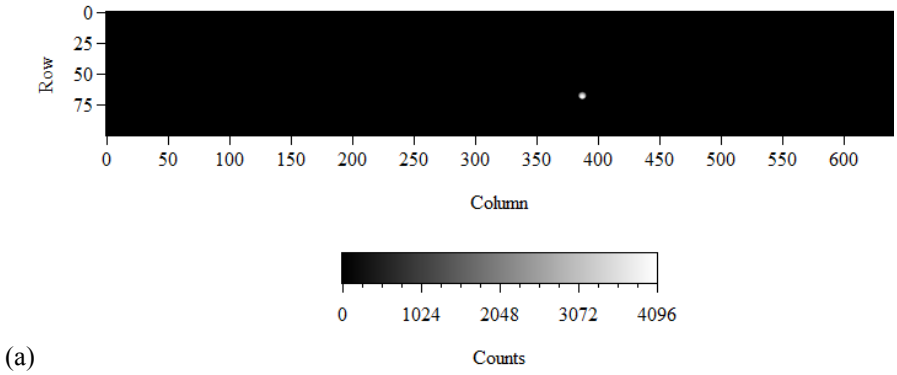


(a)

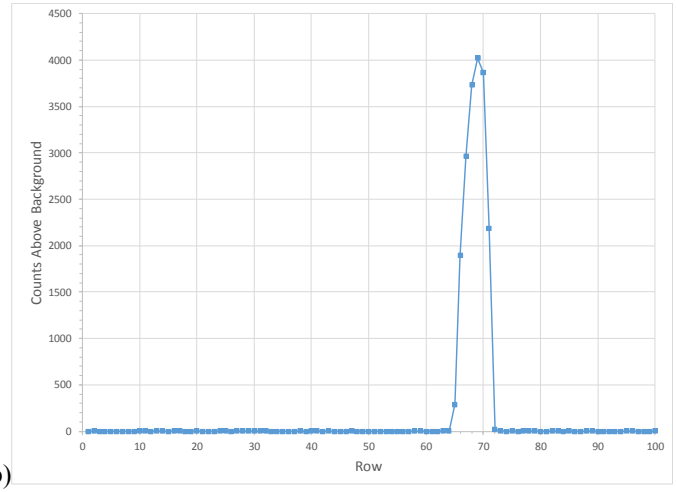


(b)

Figure 15. Simulated image of the full moon (a) from the 2.25 µm band and the signal profile (b) from the image showing high SNR.

## 9. SUMMARY AND CONCLUSIONS

In this paper we have described a new instrument, CMIS, being designed and built by JHU/APL to fill a need for a small, compact yet capable MWIR imaging satellite. The instrument will use HOT MWIR detector technology and an innovative optical and mechanical design to lessen the SWaP that is typically associated with MWIR instruments. We envision that the lower cost and lower SWaP of the CMIS instrument will make it possible to deploy a constellation of these instruments in LEO to provide constant monitoring of cloud heights, temperatures and wind patterns that will enable more accurate weather forecasting in the future. The program is currently in the preliminary design phase with an airborne demonstration flight scheduled for the Fall of 2019.

We gratefully acknowledge that this work has been made possible by NASA Grant NNX17AB65G/125182.

## REFERENCES

[1] National Academies of Sciences, Engineering, and Medicine. 2018. Thriving on Our Changing Planet: A Decadal Strategy for Earth Observation from Space. Washington, DC: The National Academies Press., https://doi.org.10.17226/24938.

[2] B. A. Baum, R. F. Arduini, B. A. Wielicki, P. Minnis and S-C Tsay, Multilevel cloud retrieval using multispectral HIRS and AVHRR data: Nighttime oceanic analysis, *J. Geophys. Res.*, 99. D3, 5499-5514, (1994).

[3] Frey, R. A., B. A. Baum, W. P. Menzel, S. A. Ackerman, C. C. Moeller, and J. D. Spinhirne, A comparison of cloud top heights computed from airborne lidar and MAS radiance data using CO2 slicing, *J. Geophys. Res.*, **104**, 24,547–24,556. (1999),

[4] NRC, 2007: Earth Science and Applications from Space: National Imperatives for the Next Decade and Beyond., The National Academies Press, 456 pp.

[5] Cess, R. D., et al, Interpretation of cloud-climate feedback as produced by 14 atmospheric general circulation models. Science, 245, 513–516 (1989), doi:10.1126/science.245.4917.513.

[6] Bellomo, K., A. C. Clement, J. R. Norris, and B. J. Soden, Observational and model estimates of cloud amount feedback over the Indian and Pacific Oceans. J. Climate, 27, 925–940 (2014), doi:10.1175/JCLI-D-13-00165.1.

[7] Calisto, M., D. Folini, M. Wild, and L. Bengtsson, Cloud radiative forcing inter-comparison between fully coupled CMIP5 models and CERES satellite data. Ann. Geophys., 32, 793–807 (2014), doi:10.5194/angeo-32-793-2014.

[8] Myers, T. A., and J. R. Norris, Reducing the uncertainty in subtropical cloud feedback, Geophys. Res. Lett., 43 (2016), 2144–2148, doi:10.1002/2015GL067416.

[9] L. Esaki and R. Tsu, "Superlattice and Negative Differential Conductivity in Semiconductors," IBM J. Res. Dev. **14**, 61 (1970).

[10] W.E. Tennant, D. Lee, M. Zandian, E. Piquette, and M. Carmody, "Rule 07, a Good Heuristic Predictor of p/n HgCdTe Photodiode Performance," J. Electron. Mater. 37, 1406 (2008).

[11] https://www.flir.com/products/isc0403/.

[12] Raghu Kacker and Howard Yoon, Guidelines for Radiometric Calibration of Electro-Optical Instruments for Remote Sensing, National Institute for Standards and Technology, NIST HB 157, p. 1, May 2015.

[13] CI-Systems METS: https://www.ci-systems.com/large-aperture-collimators-flir-Tester

[14] Electro-Optical Industries: https://www.electro-optical.com.

[15] Gooch and Housego: http://www.ghinstruments.com/products/integrating-spheres/.

[16] Spectral Products: http://www.spectralproducts.com/dk240.html.

[17] SE-IR Corporation: http://www.seir.com.

[18] J. K. Henriksen Corporation, http://www.cryotestsystems.com.

[19] Reference 9, p. 81-83.

[20] Reference 9, p. 83-84.